iScience

CellPress
OPEN ACCESS

Article

Enhanced photocatalytic activity and mechanism insight of copper-modulated lead-free $Cs_2AgSbCl_6$ double perovskite microcrystals

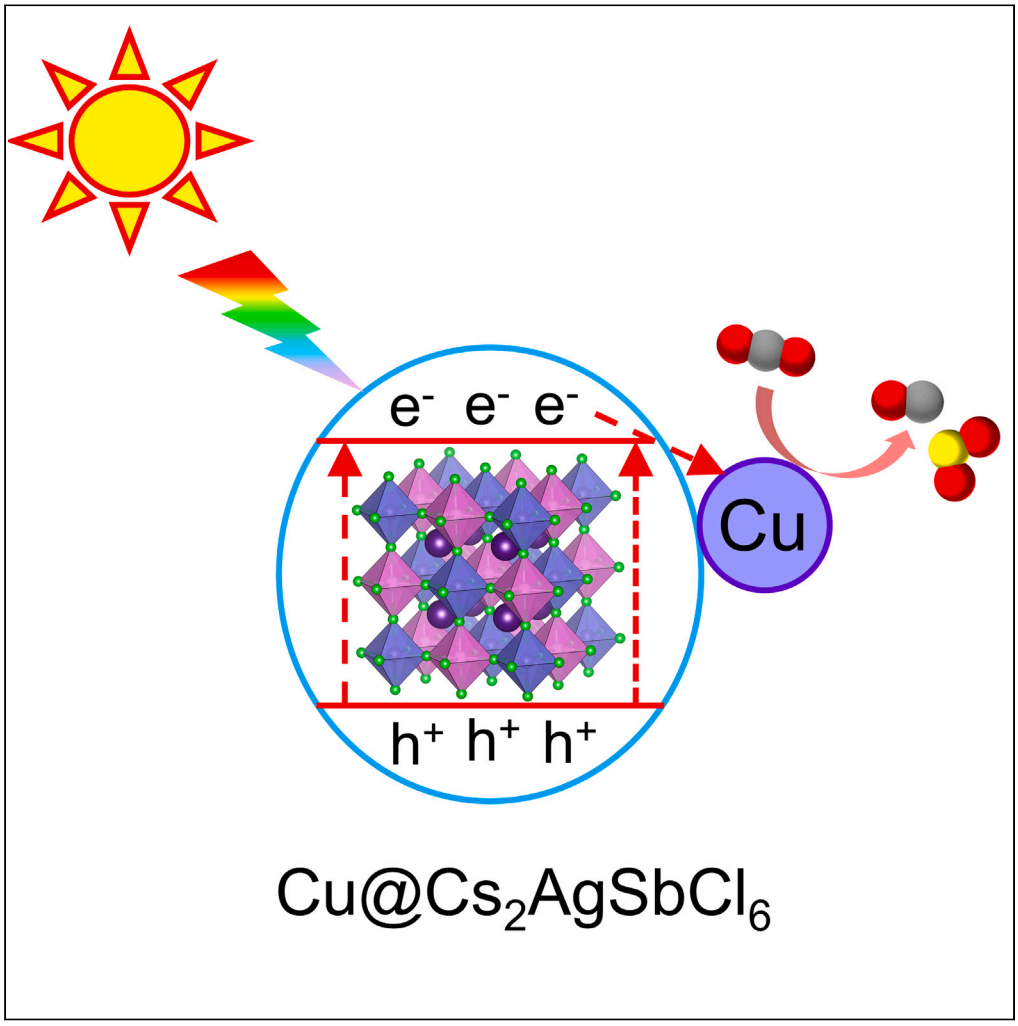

Daofu Wu, Xiaoqing Liu, Changqing Tian, ..., Miao Zhou, Qiang Huang, Xiaosheng Tang

mzhou@cqu.edu.cn (M.Z.)
huangqiang@cqupt.edu.cn (Q.H.)
xstang@cqu.edu.cn (X.T.)

Highlights

Cu-doped $Cs_2AgSbCl_6$ catalyst is successfully constructed

Excellent activity benefit from the Cu site

Cu regulation effect on the photocatalytic performance is revealed

Wu et al., iScience 26, 107355
August 18, 2023
https://doi.org/10.1016/j.isci.2023.107355

iScience

CellPress
OPEN ACCESS

Article

Enhanced photocatalytic activity and mechanism insight of copper-modulated lead-free $Cs_2AgSbCl_6$ double perovskite microcrystals

Daofu Wu,[1,4] Xiaoqing Liu,[1,4] Changqing Tian,[2] Jinchen Zhou,[2] Junan Lai,[1] Hongmei Ran,[2] Bo Gao,[3] Miao Zhou,[1,*] Qiang Huang,[2,*] and Xiaosheng Tang[1,2,3,5,*]

SUMMARY

Lead halide perovskites are prospective candidates for CO_2 photoconversion. Herein, we report copper-doped lead-free $Cs_2AgSbCl_6$ double perovskite microcrystals (MCs) for gas-solid phase photocatalytic CO_2 reduction. The 0.2Cu@$Cs_2AgSbCl_6$ double perovskite MCs display unprecedented CO_2 photoreduction capability with CO and CH_4 yields of 412 and 128 μmol g^{-1}, respectively. The ultrafast transient absorption spectroscopy reveals the enhanced separation of photoexcited carriers in copper-doped $Cs_2AgSbCl_6$ MCs. The active sites and reaction intermediates on the surface of the doped $Cs_2AgSbCl_6$ are dynamically monitored and precisely unraveled based on the *in-situ* Fourier transform infrared spectroscopy investigation. In combination with density functional theory calculations, it is revealed that the copper-doped $Cs_2AgSbCl_6$ MCs facilitate sturdy CO_2 adsorption and activation and strikingly enhance the photocatalytic performance. This work offers an in-depth interpretation of the photocatalytic mechanism of $Cs_2AgSbCl_6$ doped with copper, which may provide guidance for future design of high-performance photocatalysts for solar fuel production.

INTRODUCTION

As the consumption of fossil fuels increases rapidly, the global warming induced by the excessive discharging of carbon dioxide (CO_2) gas has become a huge challenge of the new century.[1,2] Photocatalytic conversion of CO_2 is generally perceived as one of the most judicious avenues to simultaneously tackle both energy demand and environmental issues. In a typical light-driven CO_2 reduction process, the photogenerated charge carriers are firstly formed upon light irradiation and then migrate to the catalytically active sites to participate in reduction and oxidation reactions with the surface-adsorbed reactants.[3,4] Thus, the photoelectric properties and catalytic centers of photocatalysts play crucial roles in the conversion efficiency and product selectivity.[5,6] Therefore, it is highly desirable to develop an efficient photocatalyst with superior photoelectric characteristics and abundant reaction sites.

Among various semiconductor materials, the lead halide perovskites have attracted widespread attention for their applications on photodetectors, light-emitting diodes, solar cells, etc.[7–12] However, the toxic Pb and crystal instability inhibit the practical application of Pb-halide perovskites. In this regard, lead-free perovskites that replace Pb^{2+} in the perovskite structure with nontoxic metal ions have become a current research hotspot. The lead-free double perovskite with a general formula of $A_2Z'Z''X_6$, which combines a lead-free trivalent (Z′) and monovalent (Z″) cation pairs to replace the B-site cations, exhibits distinctive performance. Compared to the conventional ABX_3 perovskites, $A_2Z'Z''X_6$ double perovskites with a similar three-dimensional perovskite structure display enhanced air and moisture stability.[13–19] The B-site cation is usually substituted through the following cation pairs: Ag^+/Bi^{3+}, Ag^+/In^{3+}, Ag^+/Sb^{3+}, or Cu^+/In^{3+}, etc.[13–23] For example, the $Cs_2AgSbCl_6$ crystals with a varied band gap have been prepared by Zhou et al.,[24] and a kind of $Cs_2AgSbCl_6/TiO_2$ heterojunction was demonstrated to exhibit effective separation of photogenerated carriers.[25] Furthermore, visible-light-driven photocatalytic C−C bond forming was achieved via using lead-free double perovskite $Cs_2AgSbCl_6$ nanocrystals, which showed significant potential applications in the field of photocatalysis.[26]

[1]Key Laboratory of Optoelectronic Technology & Systems (Ministry of Education), College of Optoelectronic Engineering, Chongqing University, Chongqing 400044, China

[2]College of Optoelectronic Engineering, Chongqing University of Posts and Telecommunications, Chongqing 400065, China

[3]School of Materials Science and Engineering, Zhengzhou University, Zhengzhou 450001, China

[4]These authors contributed equally

[5]Lead contact

*Correspondence: mzhou@cqu.edu.cn (M.Z.), huangqiang@cqupt.edu.cn (Q.H.), xstang@cqu.edu.cn (X.T.)

https://doi.org/10.1016/j.isci.2023.107355

In addition to the search of new double perovskites with different components or structures, various strategies have been proposed to tune the physical properties of perovskite materials. In particular, doping double perovskites with metal cations has attracted considerable interest as the doped materials display enhanced stability and intriguing photoelectric properties. For instance, the 0.04% Bi-doped $Cs_2(Ag_{0.60}Na_{0.40})InCl_6$ emits efficient (86% quantum efficiency) and stable (over 1,000 h) warm-white light,[27] Bi modulations of $MAPbI_3$, $Cs_2AgInBr_6$, and $Cs_2AgSbBr_6$ show enhanced stability,[17,28] and Mn dopant ameliorates the durability of $CsPbI_3$ and provokes bright orange photoluminescence emissions in $Cs_2AgInCl_6$.[29,30] Among metal dopants, Cu is one of the most widely investigated element to adjust the fundamental features of semiconductors.[31] For example, the Cu-doped perovskite enhances lattice formation energy and heightens short-range order, resulting in significant improvement of the thermal stability and optical performance.[32] Recently, K. Michaelis et al. presented the optical properties of $Cs_2AgSbCl_6$ double perovskite, which are directly related to the Cu^{2+} doping that causes a decrease of the band gap, from ~2.6 eV ($Cs_2AgSbCl_6$) to ~1 eV (Cu-doped $Cs_2AgSbCl_6$).[33] However, to the best of our knowledge, the doping effects on the photocatalytic properties of double perovskites have been rarely reported.

In this study, the Cu-doped $Cs_2AgSbCl_6$ microcrystals (MCs) are used as high-efficiency photocatalysts for the gas-solid phase CO_2 reduction reaction (CO_2RR) under 300 W Xe lamp illumination. In contrast to the pure $Cs_2AgSbCl_6$ MCs, the Cu-doped MCs show an unparalleled photocatalytic CO_2 conversion activity. Ultrafast transient absorption (TA) spectroscopy reveals that the Cu atom-induced intrinsic change of the surface trap states of $Cs_2AgSbCl_6$ is the primary factor behind the dramatically improved photocatalytic performance. Under the concrete interfacial modes, the crux reaction intermediates and parameters are detected using *in-situ* Fourier transform infrared spectroscopy (FT-IR). Furthermore, the *in-situ* experimental data are further understood by density functional theory (DFT) calculations, which reveal the fundamental mechanism of the enhanced photocatalytic performance in strengthening CO_2 adsorption and activation via inducing Cu active sites in the $Cs_2AgSbCl_6$ MCs.

RESULTS AND DISCUSSION

Structural characterization of xCu@$Cs_2AgSbCl_6$

A simple solvent synthesis method is utilized to prepare the Cu-doped $Cs_2SbAgCl_6$ double perovskite, and the corresponding samples are labeled as xCu@$Cs_2AgSbCl_6$ (x is the amount of $CuCl_2{\cdot}2H_2O$ solution). Figures 1A–1E show the field emission scanning electron microscopy (FESEM) images of the as-prepared xCu@$Cs_2AgSbCl_6$ (x = 0, 0.1, 0.2, 0.3, 0.4 mL), which display that the materials consist of multifaced micrometer-sized polycrystals. The high-resolution transmission electron microscopy (HR-TEM) image (Figure 1F) demonstrates a lattice spacing of 0.26 nm, corresponding to the (400) plane of $Cs_2SbAgCl_6$. Furthermore, the energy dispersive spectrometer (EDS) mapping images (Figure S1) confirm the existence and homogeneous distribution of Cs, Ag, Sb, Cl, and Cu elements in the 0.2Cu@$Cs_2AgSbCl_6$ MCs.

Figure S2A shows the powder X-ray diffraction (PXRD) patterns of the samples, which could be well indexed to the simulated patterns of the $Cs_2AgSbCl_6$. The magnification of the highly intense (400) peak in the PXRD patterns is shown in Figure S2B, which illustrates the shift toward higher 2θ values after Cu doping, suggesting Cu is successfully incorporated into the $Cs_2SbAgCl_6$ crystals and the average lattice parameters are decreasing for the doped materials. The X-ray photoelectron spectroscopy (XPS) results shown in Figure 1G exhibit the presence of Cs, Ag, Sb, Cl, and Cu element. The peak electron binding energy of Cl 2p shifts significantly by about 0.77 eV in the direction of higher electron binding energy after Cu doping (Figure 1K), which is caused by the introduction of Cu breaking the electronic valence balance of the original system and in order to maintain the electronic balance of the entire system. The peak electron binding energies of Cs 3d, Ag 3d, and Sb 3d remain largely unchanged after Cu doping. In particular, three peaks with peak energies of 930.11, 931.29, and 932.18 eV, which are corresponding to the $2p_{3/2}$ orbitals of Cu^0, Cu^{1+}, and Cu^{2+}, respectively, were seen in the high-resolution XPS spectrum of Cu $2p_{3/2}$. Multivalent Cu species enable selective CO_2 reduction to value-added products. Furthermore, the XPS and inductively coupled plasma-optical emission spectrometric (ICP-OES) results (Tables S1and S2) directly prove the existence of Cu element in $Cs_2SbAgCl_6$.

Photocatalytic CO_2RR activities of xCu@$Cs_2AgSbCl_6$

The photocatalytic CO_2RR activities of these xCu@$Cs_2AgSbCl_6$ MCs are further explored under the illumination of 300 W Xe lamp, and the corresponding photocatalytic performances are showed in Figure 2. After the constant irradiation for 3 h, the as-prepared 0.2Cu@$Cs_2AgSbCl_6$ MCs exhibited the CO and CH_4

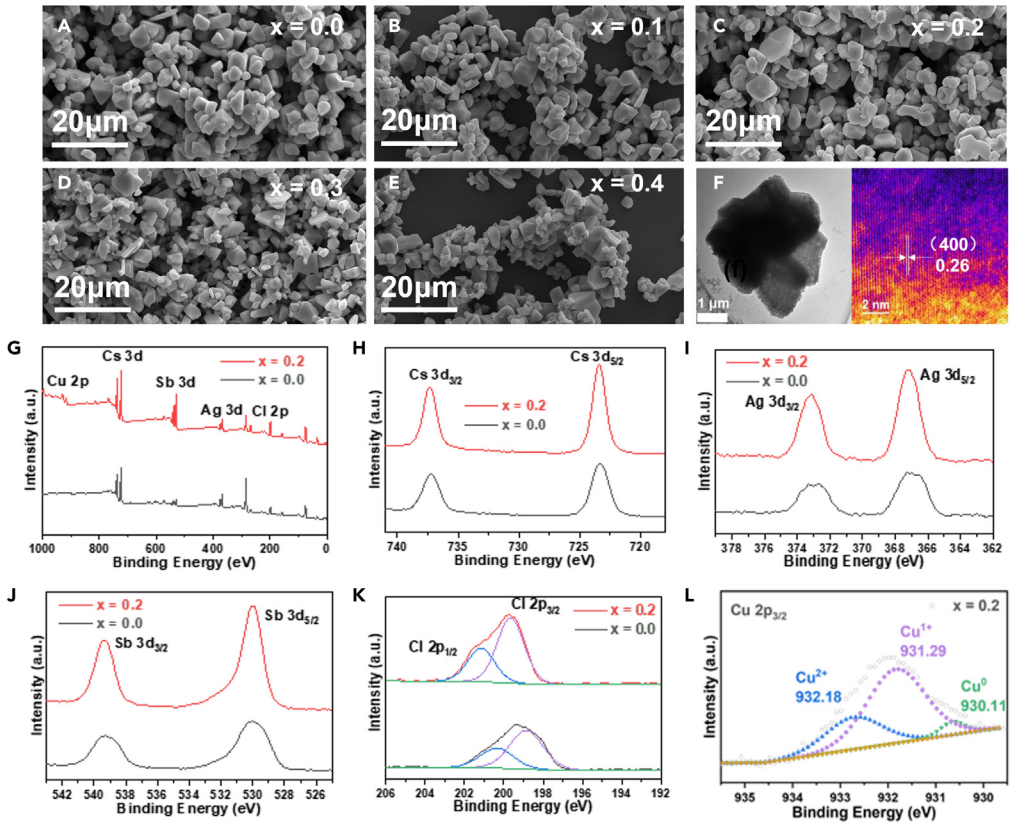

Figure 1. Morphology and chemical state

(A–E) FESEM images of xCu@$Cs_2AgSbCl_6$.

(F) TEM and HR-TEM images of $Cs_2AgSbCl_6$.

(G–L) XPS spectra of $Cs_2AgSbCl_6$ and 0.2Cu@$Cs_2AgSbCl_6$.

evolution of 412 and 128 μmol g^{-1}, respectively (Figures 2A and 2B). As a comparison, the non-doped $Cs_2AgSbCl_6$ presents CO evolution of 108 μmol g^{-1} (Figure 2A), while the corresponding CH_4 evolution is 46 μmol g^{-1} (Figure 2B). As shown in Figures 2C and 2D, the optimal 0.2Cu@$Cs_2AgSbCl_6$ achieves CO yield rate of 137 μmol g^{-1} h^{-1} and CH_4 yield rate of 43 μmol g^{-1} h^{-1}, resulting in an average electron consumption rate of 616 μmol g^{-1} h^{-1} (Figure 2D). As far as we know, the 0.2Cu@$Cs_2AgSbCl_6$ investigated here exhibits higher photocatalytic CO_2RR performance than all the previously reported pure-phase perovskite photocatalysts employed in gas-solid reaction system (Table S3). Meanwhile, the oxidation byproduct of 0.2Cu@$Cs_2AgSbCl_6$ was also investigated. The O_2 yield was 517.56 μmol/g, and the hole consumption was 2070.24 μmol/g (Figure S3).

It is crucial to identify the source of the products since organic solvents are utilized in the creation of photocatalysts and organic compounds are likely to be oxidized to CO or CH_4 under light irradiation. In order to determine the origin of the products, we conducted the isotope-labeling experiments using $^{13}CO_2$ as the reaction gas. Figure S4 demonstrates that 95% of all CO products were in the form of ^{13}CO, indicating that this process mostly converted the reactive gas CO_2 rather than oxidized organic solvents. Additionally, the products contained $^{13}CH_3$ and $^{13}CH_4$, which is evidence that CH_4 was produced.

Photocatalysts must be photochemically and structurally stable in order to be used in practical applications. As a result, we looked into 0.2Cu@$Cs_2AgSbCl_6$ MCs' stability following catalytic testing. The principal X-ray diffraction (XRD) characteristic diffraction peak positions remained mostly constant following the photocatalytic trials, as displayed in Figure S5A, demonstrating that 0.2Cu@$Cs_2AgSbCl_6$ has a sound structural stability. After photocatalytic testing, as shown in Figure S5B, the morphology of 0.2Cu@$Cs_2AgSbCl_6$ was essentially the same as that of the original 0.2Cu@$Cs_2AgSbCl_6$ (Figure 1C). In conclusion, the 0.2Cu@$Cs_2AgSbCl_6$ MCs have very good structural and morphological stability.

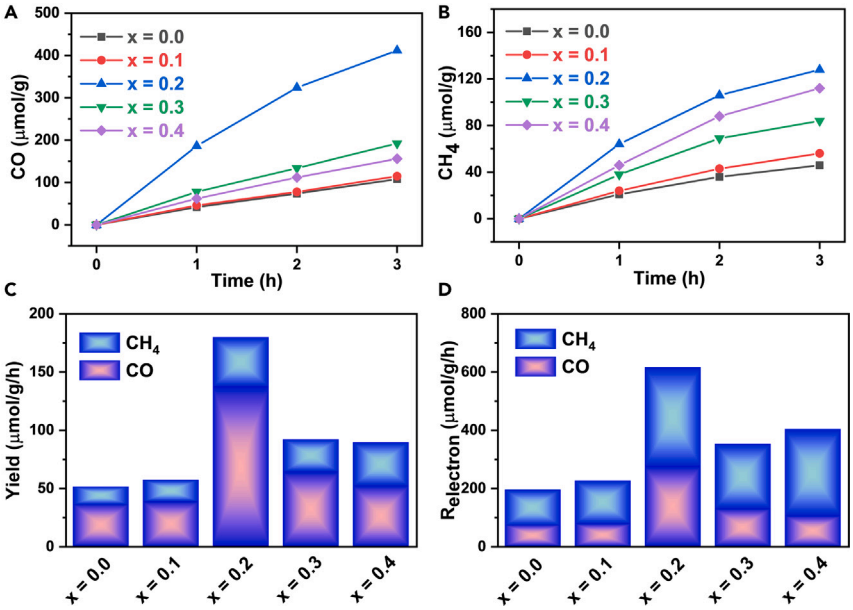

Figure 2. Photocatalytic performance CO and (B) CH_4 evolutions based on xCu@$Cs_2AgSbCl_6$

(A) Histogram of (C) the evolutions yield rate and (D) photocatalytic electron consumption rate using the xCu@$Cs_2AgSbCl_6$ as the photocatalysts.

Photoelectric properties of xCu@$Cs_2AgSbCl_6$

To gain the physical origins for the sharp enhancement of the Cu-doped $Cs_2AgSbCl_6$ in photocatalytic CO_2RR activity, the photoelectric properties of the xCu@$Cs_2AgSbCl_6$ are further investigated. Figures 3A and 3B show the calculated total and partial density of states (PDOS) for $Cs_2AgSbCl_6$ (400) and Cu@$Cs_2AgSbCl_6$ (400). Clearly, $Cs_2AgSbCl_6$ (400) is a typical semiconductor with a band gap of 1.245 eV, where the conduction (valence) band edges mainly come from 3*p* orbital of Cl. For Cu@$Cs_2AgSbCl_6$ (400), with a band gap of 0.732 eV, valence band edges are contributed by the 3*d* orbitals of Cu atoms, and conduction band edges mainly come from the 3*p* orbitals of Cl atoms. Moreover, the presence of Cu-3*d* states near the Fermi level reduces the band gap and thus enhances the catalytic activity of CO_2RR. Figure 3C shows the absorbance spectra of the pristine and Cu-doped $Cs_2SbAgCl_6$ double perovskites, indicating a dramatic enhanced absorption in relevant visible region upon Cu doping, which is consistent with the previous DFT results. The photocurrent density of the 0.2Cu@$Cs_2AgSbCl_6$ is higher than that of the pristine $Cs_2AgSbCl_6$ (Figure 3D), which greatly confirms the strengthened transfer of the charge carries in 0.2Cu@$Cs_2AgSbCl_6$. As shown in Figure 3E, the Nyquist plots indicate that the charge-transfer resistance is slightly diminished for 0.2Cu@$Cs_2AgSbCl_6$ in comparison to $Cs_2AgSbCl_6$.

As an effective tool to track the real-time photoexcited charge carrier dynamics involved in the photocatalytic process, the ultra TA spectroscopy could gain insights into the effect of elemental doping on the charge separation inside the semiconductors.[34,35] In the TA measurements, the pump light is generated by injecting the femtosecond (fs) laser from the Ti: sapphire amplifier to the optical parametric amplifier, while the probe light is generated by injecting the 800 nm pulses (1 kHz) into sapphire crystals, thus generating smooth super continuum (see details in Supporting Information). The center wavelength of the pump pulses is set at 365 nm, which could effectively promote electrons from the valence band to the conduction band of xCu@$Cs_2AgSbCl_6$. Notably, the TA kinetics for $Cs_2AgSbCl_6$ MCs has been altered after Cu doping (Figures 4A, 4B, 4D, and 4E). In Figure 4C, the pristine $Cs_2AgSbCl_6$ MCs exhibit an absorption signal of excited states, which could be described by two exponential recovery processes: τ_1 = 23.06 $\pm$ 4.57 ps (45%) and τ_2 = 0.72 $\pm$ 0.23 ps (55%), and the weighted average lifetime is 10.98 ps. The Cu-doped $Cs_2AgSbCl_6$ MCs display absorption signals of excited states as shown in Figure 4F, which could also be depicted by two exponential recovery processes: τ_1 = 25.67 $\pm$ 2.92 ps (52%) and τ_2 = 0.57 $\pm$ 0.15 ps (48%), while the weighted average lifetime is 13.28 ps. It is worth noting that the average recovery lifetime

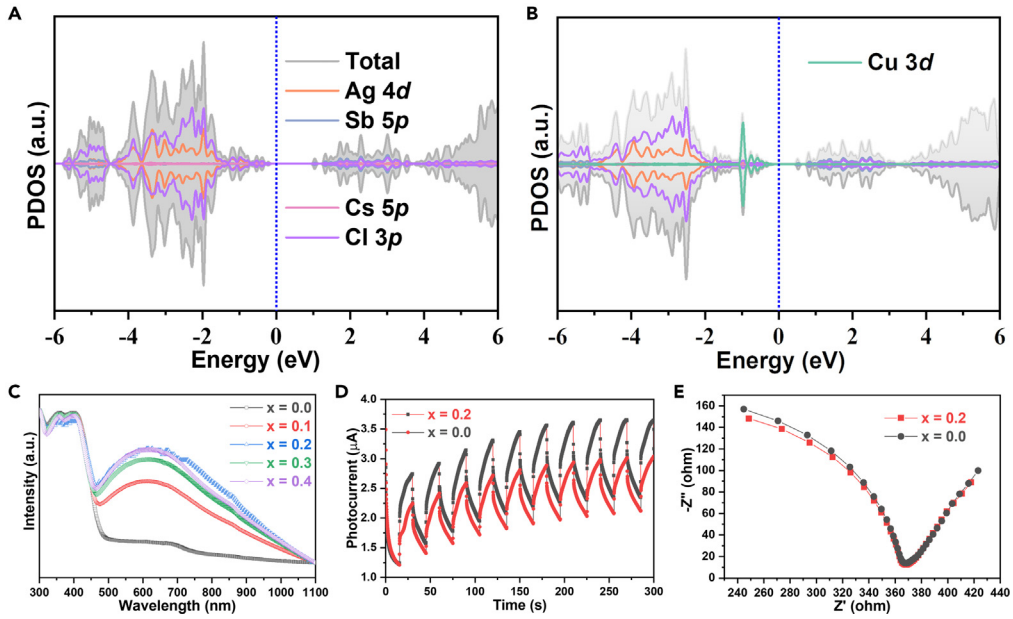

Figure 3. Photoelectric properties

(A and B) Calculated total and partial density of state of $Cs_2AgSbCl_6$ and Cu@$Cs_2AgSbCl_6$.

(C) Absorption spectra of xCu@$Cs_2AgSbCl_6$.

(D) Transient photocurrent responses and (E) Nyquist plots of $Cs_2AgSbCl_6$ and 0.2Cu@$Cs_2AgSbCl_6$ at 0.1 $V_{Ag/AgCl}$ under Xe lamp irradiation in ethyl acetate solution containing 0.1 M tetrabutylammonium hexafluorophosphate ($TBAPF_6$).

is thought of as an eventful parameter to assess the separation and transfer of the photoexcited carriers in the photocatalysts. Accordingly, the average recovery lifetime for Cu-doped $Cs_2AgSbCl_6$ is reckoned to be 13.28 ps, which is approximately 1.21 times longer than that of the pristine $Cs_2AgSbCl_6$ (10.98 ps), evidencing that the Cu doping in $Cs_2AgSbCl_6$ could bring about central improvement in the electron-hole separation efficiency. Based on the typical observation from TA kinetics, such a lifetime increase is mainly attributed to the formation of dopant energy levels of Cu in the band gap of $Cs_2AgSbCl_6$, which is consistent with the aforementioned results in the DFT calculations (Figure 3B). Especially, after the photoexcited carriers are produced in the Cu-doped $Cs_2AgSbCl_6$, the photoexcited electrons are inclined to be captured by the new trap states, which dramatically promotes the separation of the photoinduced electron-hole pairs. Thus, the new trap states resulting from Cu doping could furnish more chances for photoexcited electrons to engage in the CO_2RR.

Mechanistic analysis of CO_2RR

The effective adsorption and activation of CO_2 molecules on the photocatalyst surface are highly significant in the multielectron photoreduction process. Thus, *in-situ* FT-IR is carried out for identifying and dynamically monitoring the reaction intermediate species during CO_2 adsorption, activation, and photoconversion on xCu@$Cs_2AgSbCl_6$. As shown in Figure 5, the *in-situ* FT-IR spectra certify that several carbonates and active $\cdot CO_2^-$ intermediates are formed on the surface of xCu@$Cs_2AgSbCl_6$ during the humid CO_2 adsorption process in dark. And, the adsorption peaks at about 1,640~1,676 cm^{-1} are attributed to the characteristic vibration mode of $\cdot CO_2^-$.[36,37] Extraordinarily, the observation of $\cdot CO_2^-$ signifies that the adsorbed CO_2 molecules are activated on the surface of xCu@$Cs_2AgSbCl_6$. The peaks at around 2,343, 2,354, and 2,366 cm^{-1} are ascribed to $\nu_3(CO_2)$ of the CO_2 molecular,[38] while the bands of the adsorbed gas-phase CO_2 (around 3,597, 3,611, 3,687, and 3,713 cm^{-1}) are also detected, accompanied with the appearance of surface-bonded OH^- split from the adsorbed H_2O (~3,500 cm^{-1}).[39] Interestingly, the signals of CO_2 on the surface of the 0.2Cu@$Cs_2AgSbCl_6$ are more intensive than those on $Cs_2AgSbCl_6$ (Figure S6), which means that the presence of Cu element could not only provide more active sites for CO_2 adsorption/activation but also transform the adsorption/activation modes of CO_2. Furthermore, the peaks around 1,590, 1,540, and 1,368 cm^{-1} belong to the bidentate carbonate species (b-CO_3^{2-}).[36,39] Additionally, the peaks at 1,432, 1,340, 1,577, 1,645, and 1,480 cm^{-1} go into the monodentate carbonate (m-CO_3^{2-}),[36–38] and the peaks

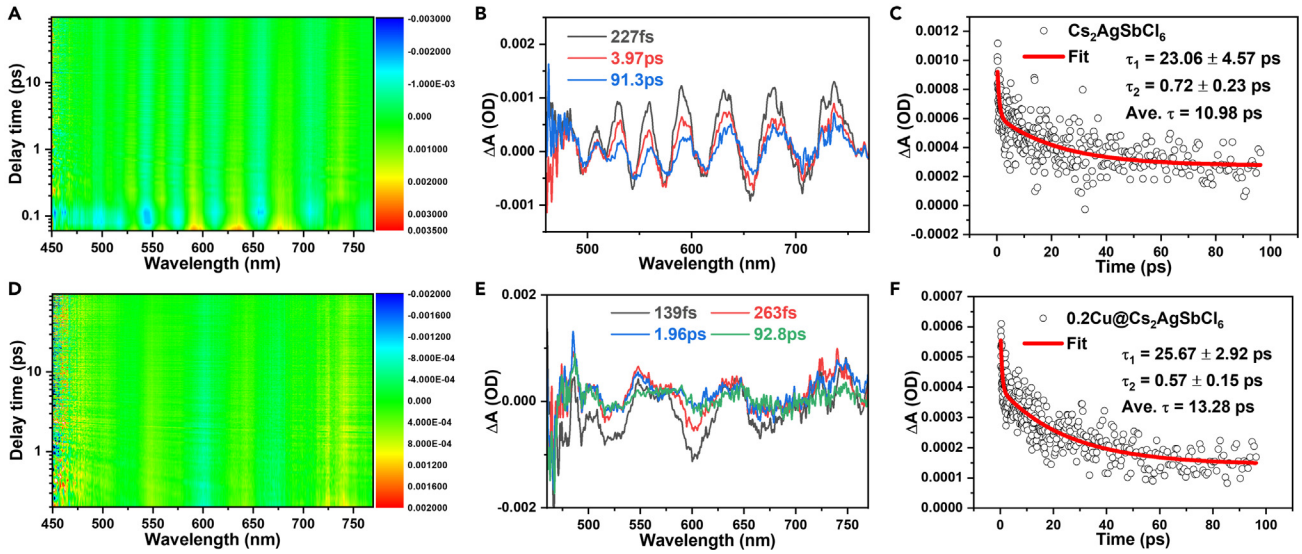

Figure 4. Ultrafast TA spectra

Contour plots of the ultrafast TA spectra of (A) $Cs_2AgSbCl_6$ and (D) 0.2Cu@$Cs_2AgSbCl_6$ upon excitation with a 365 nm fs-pulsed laser. TA spectra of (B) $Cs_2AgSbCl_6$ and (E) 0.2Cu@$Cs_2AgSbCl_6$. Representative ultrafast TA kinetics probed at 559 nm (C) $Cs_2AgSbCl_6$ and (F) at 550 nm 0.2Cu@$Cs_2AgSbCl_6$.

at 1,735 and 1,724 cm^{-1} correspond to chelating-bridged carbonate (c-CO_3^{2-}).[36] The presence of various carbonate species is caused by the formation of carbonic acid and/or adsorbed CO_2 on the photocatalyst surface. Besides, the peaks located at 1,631, 1,432, 1,340 cm^{-1}, and 1,298-1,263 cm^{-1} are reported to be bicarbonates (HCO_3^-), which grow from the interaction of the adsorbed CO_2 and H_2O at the surface.[3,39,40] Both carbonate and bicarbonate species are the considerable intermediates, which transform into product CO.[41]

As shown in Figure 5G, the $Cs_2AgSbCl_6$ structure is a typical double perovskite framework of corner-shared [$AgCl_6$] and [$SbCl_6$] octahedra and the Cs atom is located in the cavity of the octahedra. After geometry optimization, the lattice parameters of bulk $Cs_2AgSbCl_6$ are a = b = 10.85 Å, which are in accordance with previous theoretical and experimental results.[25,42] The HR-TEM has shown that the most exposed facet in $Cs_2AgSbCl_6$ is 400 plane; therefore, it has been chosen as the theoretical surface model for the following DFT calculations. The lattice of $Cs_2AgSbCl_6$ (400) (Figure S7A) is a = b = 10.62 Å, and the average lattice parameters of Cu@$Cs_2AgSbCl_6$ (400) decrease with the increase of doped copper content (Figures S7 and S8), which is consistent with the previous XRD results (Figure S2).

To further study the catalytic activity of CO_2RR, we calculate the d-band center and charge transfer and adsorption energies of CO_2 adsorption on $Cs_2AgSbCl_6$ (400) and Cu@$Cs_2AgSbCl_6$ (400). As an active site, Ag atom exhibits relatively weak CO_2 adsorption strength with an adsorption energy of −0.14 eV. After Cu doping, CO_2 is bonded to Cu atom with adsorption energy of −0.56 eV, which is much stronger than the adsorption on the pristine surface, consistent with the previous *in-situ* FT-IR results (Figure S6B). Although the negative adsorption energies of $Cs_2AgSbCl_6$ (400) and Cu@$Cs_2AgSbCl_6$ (400) indicate that spontaneous CO_2 adsorption could occur, the Cu atom is a superior activation site for CO_2 adsorption compared to Ag. Moreover, the d-band center of Cu@$Cs_2AgSbCl_6$ is −2.03 eV, which is higher than that of $Cs_2AgSbCl_6$(400) (−2.54 eV), as shown in Table S5. Therefore, both experiments and DFT calculations suggest incorporating an Ag atom in $Cs_2AgSbCl_6$ by replacing a corner Cu atom upshifting the d-band center closer to the Fermi level, which boosts the CO_2 adsorption and activation. As shown in Figures 5H and 5I, the electron transfer from Ag to CO_2 molecules and from Cu to CO_2 in Cu@$Cs_2AgSbCl_6$ (400) is observed, while minimal electron transfer is observed in $Cs_2AgSbCl_6$ (400). Bader charge analysis[43,44] shows that Cu@$Cs_2AgSbCl_6$ (400) loses charge 0.85 *e* (from Cu atom to CO_2 atom), which is higher than that of $Cs_2AgSbCl_6$ (400) (0.80 *e*) (from Ag atom to CO_2 atom), indicating that CO_2 adsorption on Cu@$Cs_2AgSbCl_6$ (400) is easily further hydrogenated to form *CO intermediate. This demonstrates

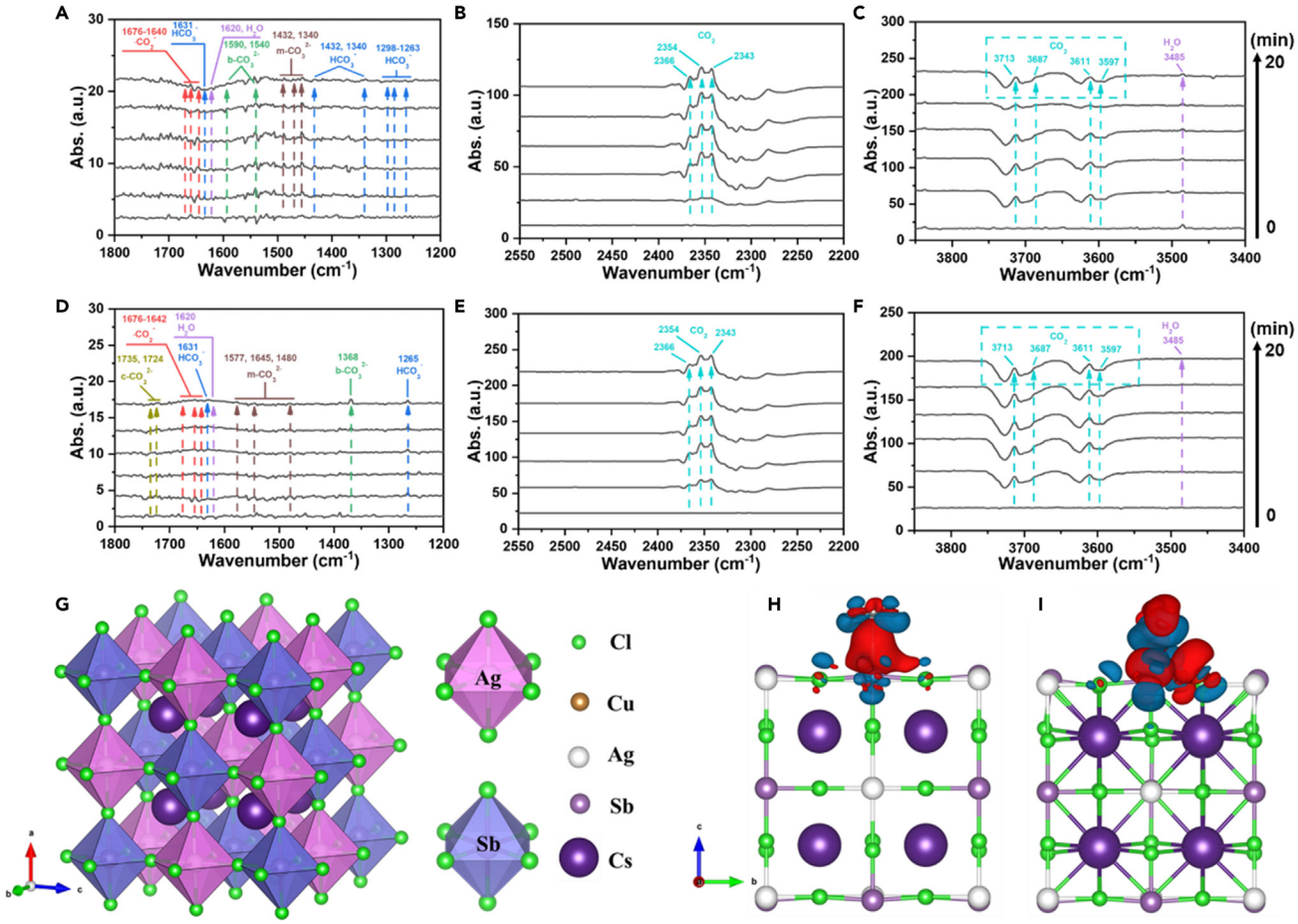

Figure 5. *In-situ* FT-IR tests and charge difference density

In-situ FT-IR tests for CO_2 and H_2O interaction with $Cs_2AgSbCl_6$ (A–C) and 0.2Cu@$Cs_2AgSbCl_6$ (D–F) in the dark.

(G) Schematic of bulk $Cs_2AgSbCl_6$ double perovskite with NaCl-type lattice. Octahedra of [$AgCl_6$] and [$SbCl_6$] are highlighted. The charge difference density of (H) $Cs_2AgSbCl_6$(400) and (I) Cu@$Cs_2AgSbCl_6$(400) with CO_2 adsorption (isovalue = 1 × 10^{-4} e/Å^3). The red and blue color represent charge accumulation and depletion, respectively.

stronger reducibility of the Cu active sites in Cu@$Cs_2AgSbCl_6$ (400) compared to Ag active sites in $Cs_2AgSbCl_6$ (400).

The evolution of surface-bonded species on the xCu@$Cs_2AgSbCl_6$ surface under Xe lamp irradiation is evaluated based on *in-situ* FT-IR (Figure 6). These peaks of carbonate species, involving CO_3^{2-} (1,544, 1,510, 1,454, and 1,377 cm^{-1}) and HCO_3^- (1,474, 1,417, 1,410, and 1,295-1,264 cm^{-1}),[36,37,45,46] affirm that the adsorbed and activated species are depleted and instantly converted (Figures 5A and 5C). Then, the peaks of *COOH (1,737, 1,578, and 1,556 cm^{-1}), CO* (1,719 cm^{-1}), and $\cdot CO_2^-$ (1,685 and 1,609 cm^{-1}) emerge and raise in intensity over time.[37,47,48] The discovery of *COOH and CO* directly proves that the light illumination of xCu@$Cs_2AgSbCl_6$ results in subsequent multistep hydrogenation of $\cdot CO_2^-$ radicals to generate CO. In addition, the high-wavenumber region of the FT-IR results demonstrates that numerous intermediates are formed during the photocatalytic reaction, incorporating CH_3O* (2,848 cm^{-1}) and CH_2* (2,870, 2,912, 2,917, 2,946, and 2,936 cm^{-1}) (Figures 6B and 6D).[49–53] The existence of the staple CH_x* species suggests the formation of CH_4 on the xCu@$Cs_2AgSbCl_6$ surface. On the ground of these *in situ* FT-IR results, the reaction routes for CO_2 photoreduction on xCu@$Cs_2AgSbCl_6$ are proposed (see the Supporting Information).

To theoretically understand the $Cs_2AgSbCl_6$ and Cu@$Cs_2AgSbCl_6$ for CO_2RR, we perform DFT calculations for the Gibbs free energy diagram based on the computational hydrogen electrode model (For details, see

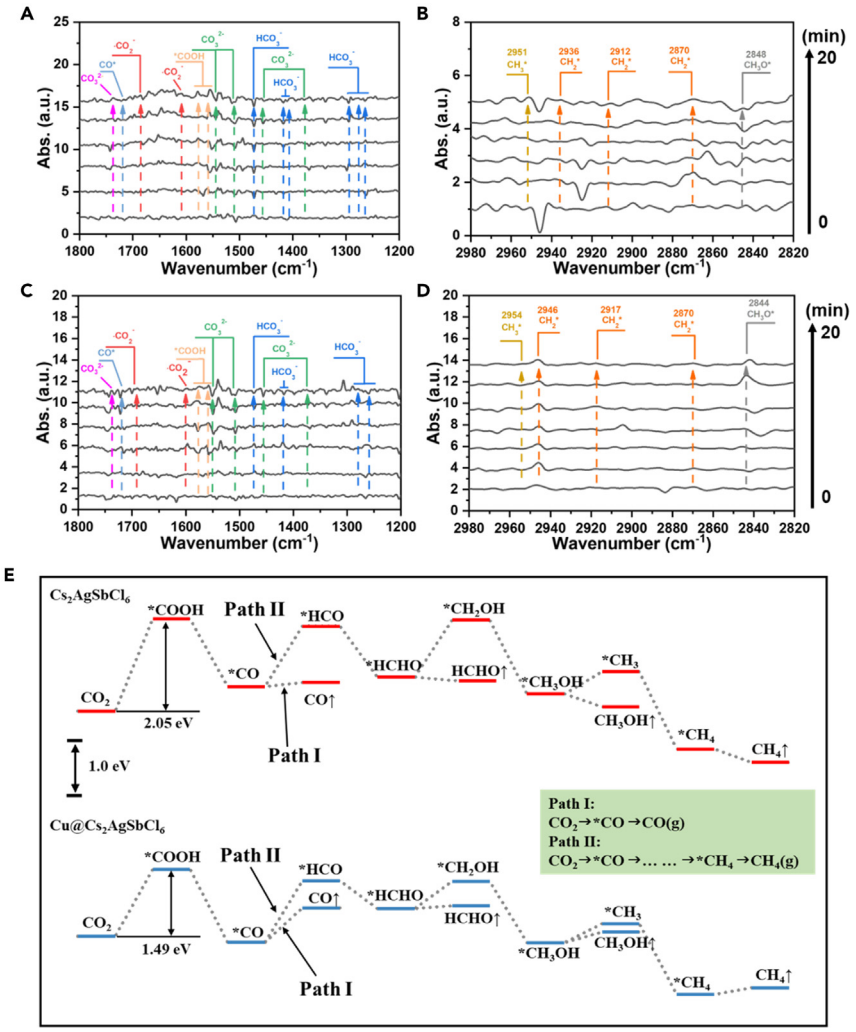

Figure 6. *In-situ* FT-IR tests and Gibbs free energy diagram

In-situ FT-IR tests of CO_2 and H_2O interaction with $Cs_2AgSbCl_6$ (A and B) and 0.2Cu@$Cs_2AgSbCl_6$ (C and D) under constant 300 W Xe lamp illumination.

(E) Calculated Gibbs free energy diagram for CO_2RR on $Cs_2AgSbCl_6$ and Cu@$Cs_2AgSbCl_6$.

Supporting Information, Table S4).[54] As shown in Figure 6E, the formation of *COOH on the active site, involving the first proton-coupled electron transfer (CO_2+*+H^++e^-→*COOH), is the rate-determining step (RDS) due to its largest energy barrier. Less energy barrier (1.49 eV) is required for Cu@$Cs_2AgSbCl_6$ to realize the transformation of CO_2 to *COOH compared to that for $Cs_2AgSbCl_6$ (2.05 eV), implying higher CO_2RR catalytic activity. Further hydrogenation of *CO is a critical step for forming CH_4. In contrast to the hydrogenation (*CO + H^++e^-→*HCO) step, the desorption of CO (*CO→CO+*) preferentially occurs on *CO intermediate for $Cs_2AgSbCl_6$ and Cu@$Cs_2AgSbCl_6$ due to the energy favorability. This is attributed to the high energy barrier that weakens the binding strength of *CO species due to insufficient single-site activation and the low d-band position. Thus, the main photoreduction product for $Cs_2AgSbCl_6$ and Cu@$Cs_2AgSbCl_6$ is mainly CO. For the same reason, HCHO and CH_2OH are also easier to form than CH_4 for both $Cs_2AgSbCl_6$ and Cu@$Cs_2AgSbCl_6$. These results imply that Cu@$Cs_2AgSbCl_6$ has promising activity for CO_2RR that facilitates the two-electron reduction of CO_2 to CO.

Conclusions

In conclusion, the Cu-doped $Cs_2AgSbCl_6$ MCs are constructed for high activity in photocatalytic CO_2RR at the gas-solid interface. The combination of experimental investigations and theoretical calculations is

adopted to reveal the mechanism of copper regulation effects on the photocatalytic performance of Cu@$Cs_2AgSbCl_6$. Compared with pristine $Cs_2AgSbCl_6$, the Cu-doped $Cs_2AgSbCl_6$ possesses reduced band gap and enhanced separation of photoexcited charge carriers. The incorporation of Ag in $Cs_2AgSbCl_6$ by replacing a corner Cu atom decreases the lattice and upshifts the d-band center of Cu@$Cs_2AgSbCl_6$ closer to the Fermi level, which tremendously boosts the CO_2 conversion. The Cu active site in Cu@$Cs_2AgSbCl_6$ (400) demonstrates stronger reducibility compared to Ag active site in $Cs_2AgSbCl_6$ (400). The reaction energy of the *COOH formation from CO_2, as the rate-limiting step, can be lowered via the Cu element modulation. The high photocatalytic CO_2RR capability of Cu@$Cs_2AgSbCl_6$ to form CO and CH_4 further verifies its superb photoreduction property. This work illustrates that the surface active sites modulation on the ground of the copper regulation could act as an exceedingly brawny tool to promote the photocatalytic performance by optimizing the electronic structure and modulating CO_2 adsorption and photoreduction mechanism, which could afford substitute chances for utilizing lead-free halide perovskites in photocatalytic applications.

STAR★METHODS

Detailed methods are provided in the online version of this paper and include the following:

- KEY RESOURCES TABLE
- RESOURCE AVAILABILITY
  - Lead contact
  - Materials availability
  - Data and code availability
- METHOD DETAILS
  - Synthesis of the $Cs_2AgSbCl_6$ microcrystals
  - Synthesis of the Cu doped $Cs_2AgSbCl_6$ microcrystals
  - Characterization
  - Photocatalytic CO_2 reduction
  - Ultrafast transient absorption
  - In-situ FT-IR investigation on photocatalytic CO_2 reduction
  - Computational details

SUPPLEMENTAL INFORMATION

Supplemental information can be found online at https://doi.org/10.1016/j.isci.2023.107355.

ACKNOWLEDGMENTS

This work acquired financial support from the Fundamental Research Funds for the National Key Research and Development Program of China (Grant No. 2018YFB2200500); National Natural Science Foundation of China (61975023, 51775070, 22072010, 61875211); Guangdong Province International Scientific and Technological Cooperation Projects (grant number 2020A0505100011); CAS Interdisciplinary Innovation Team, and the Open Fund of the State Key Laboratory of High Field Laser Physics (Shanghai Institute of Optics and Fine Mechanics); Opening Project of State Key Laboratory of Advanced Technology for Float Glass; State Key laboratory of Advanced Technology for Materials Synthesis and Processing (Wuhan University of Technology, No. 2021-KF-19); Natural Science Foundation of Chongqing (Grant No. cstc2021ycjh-bgzxm0181); the Science and Technology Research Program of Chongqing Municipal Education Commission (Grant No. KJZD-K202100601); and Institute for Advanced Sciences (Grant No. E011A2022325).

AUTHOR CONTRIBUTIONS

Daofu Wu and Xiaoqing Liu contributed equally. Daofu Wu: Resources, Conceptualization, Investigation, Methodology, Writing - Original Draft; Xiaoqing Liu: Resources, Investigation, Methodology, Writing - Original Draft; Changqing Tian: Investigation; Jingchen Zhou: Investigation; Junan Lai: Investigation; Hongmei Ran: Investigation; Bo Gao: Investigation; Miao Zhou: Writing-Review & Editing, Supervision; Qiang Huang: Writing-Review & Editing, Supervision; Xiaosheng Tang: Writing-Review & Editing, Supervision.

DECLARATION OF INTERESTS

The authors declare no competing interests.

Received: December 29, 2022
Revised: April 21, 2023
Accepted: July 7, 2023
Published: July 10, 2023

REFERENCES

1. Li, N., Chen, X., Wang, J., Liang, X., Ma, L., Jing, X., Chen, D.-L., and Li, Z. (2022). ZnSe nanorods-$CsSnCl_3$ perovskite heterojunction composite for photocatalytic CO_2 reduction. ACS Nano *16*, 3332–3340.

2. Cui, Z., Wang, P., Wu, Y., Liu, X., Chen, G., Gao, P., Zhang, Q., Wang, Z., Zheng, Z., Cheng, H., et al. (2022). Space-confined growth of lead-free halide perovskite $Cs_3Bi_2Br_9$ in MCM-41 molecular sieve as an efficient photocatalyst for CO_2 reduction at the gas-solid condition under visible light. Appl. Catal., B *310*, 121375.

3. Li, X., Wang, N., Zhao, Y., Zhang, Y., Liu, Z., Xu, X., Pan, Y., Ju, H., Zhu, J., and Xie, Y. (2019). Selective visible-light-driven photocatalytic CO_2 reduction to CH_4 mediated by atomically thin $CuIn_5S_8$ layers. Nat. Energy *20*, 690–695.

4. Hu, Y., Zhan, F., Wang, Q., Sun, Y., Yu, C., Zhao, X., Wang, H., Long, R., Zhang, G., Gao, C., et al. (2020). Tracking mechanistic pathway of photocatalytic CO_2 reaction at Ni sites using Operando, time-resolved spectroscopy. J. Am. Chem. Soc. *142*, 5618–5626.

5. Zhang, L., Zhao, Z.-J., Wang, T., and Gong, J. (2018). Nano-designed semiconductors for electro- and photoelectro-catalytic conversion of carbon dioxide. Chem. Soc. Rev. *47*, 5423–5443.

6. Bjelajac, A., Kopač, D., Fecant, A., Tavernier, E., Petrović, R., Likozar, B., and Janaćković, D. (2020). Micro-kinetic modelling of photocatalytic CO_2 reduction over undoped and N-doped TiO_2. Catal. Sci. Technol. *10*, 1688–1698.

7. Zhang, J., Hodes, G., Jin, Z., and Liu, S.F. (2019). All-inorganic $CsPbX_3$ perovskite solar cells: progress and prospects. Angew. Chem. Int. Ed. Engl. *58*, 15596–15618.

8. Min, H., Lee, D.Y., Kim, J., Kim, G., Lee, K.S., Kim, J., Paik, M.J., Kim, Y.K., Kim, K.S., Kim, M.G., et al. (2021). Perovskite solar cells with atomically coherent interlayers on SnO_2 electrodes. Nature *598*, 444–450.

9. Zhu, L., Cao, H., Xue, C., Zhang, H., Qin, M., Wang, J., Wen, K., Fu, Z., Jiang, T., Xu, L., et al. (2021). Unveiling the additive-assisted oriented growth of perovskite crystallite for high performance light-emitting diodes. Nat. Commun. *12*, 5081.

10. Liu, Z., Qiu, W., Peng, X., Sun, G., Liu, X., Liu, D., Li, Z., He, F., Shen, C., Gu, Q., et al. (2021). Perovskite light-emitting diodes with EQE exceeding 28% through a synergetic dual-additive strategy for defect passivation and nanostructure regulation. Adv. Mater. *33*, 2103268.

11. Sulaman, M., Yang, S., Bukhtiar, A., Tang, P., Zhang, Z., Song, Y., Imran, A., Jiang, Y., Cui, Y., Tang, L., and Zou, B. (2022). Hybrid bulk-heterojunction of colloidal quantum dots and mixed-halide perovskite nanocrystals for high-performance self-powered broadband photodetectors. Adv. Funct. Mater. *32*, 2201527.

12. Wang, H.-P., Li, S., Liu, X., Shi, Z., Fang, X., and He, J.-H. (2021). Low-dimensional metal halide perovskite photodetectors. Adv. Mater. *33*, 2003309.

13. McClure, E.T., Ball, M.R., Windl, W., and Woodward, P.M. (2016). Cs_2AgBiX_6 (X = Br, Cl): new visible light absorbing, lead-free halide perovskite semiconductors. Chem. Mater. *28*, 1348–1354.

14. Nakajima, T., and Sawada, K. (2017). Discovery of Pb-free perovskite solar cells via high-throughput simulation on the K computer. J. Phys. Chem. Lett. *8*, 4826–4831.

15. Volonakis, G., Haghighirad, A.A., Milot, R.L., Sio, W.H., Filip, M.R., Wenger, B., Johnston, M.B., Herz, L.M., Snaith, H.J., and Giustino, F. (2017). $Cs_2InAgCl_6$: a new lead-free halide double perovskite with direct band gap. J. Phys. Chem. Lett. *8*, 772–778.

16. Slavney, A.H., Hu, T., Lindenberg, A.M., and Karunadasa, H.I. (2016). A bismuth-halide double perovskite with long carrier recombination lifetime for photovoltaic applications. J. Am. Chem. Soc. *138*, 2138–2141.

17. Du, K.Z., Meng, W., Wang, X., Yan, Y., and Mitzi, D.B. (2017). Bandgap engineering of lead-free double perovskite $Cs_2AgBiBr_6$ through trivalent metal alloying. Angew. Chem. Int. Ed. Engl. *56*, 8158–8162.

18. Slavney, A.H., Leppert, L., Bartesaghi, D., Gold-Parker, A., Toney, M.F., Savenije, T.J., Neaton, J.B., and Karunadasa, H.I. (2017). Defect-induced band-edge reconstruction of a bismuth-halide double perovskite for visible-light absorption. J. Am. Chem. Soc. *139*, 5015–5018.

19. Tran, T.T., Panella, J.R., Chamorro, J.R., Morey, J.R., and McQueen, T.M. (2017). Designing indirect-direct bandgap transitions in double perovskites. Mater. Horiz. *4*, 688–693.

20. Yang, B., Hong, F., Chen, J., Tang, Y., Yang, L., Sang, Y., Xia, X., Guo, J., He, H., Yang, S.Q., et al. (2019). Colloidal synthesis and charge-carrier dynamics of $Cs_2AgSb_{1-y}Bi_yX_6$ (X: Br, Cl, 0 <= y <= 1) double perovskite nanocrystals. Angew. Chem. Int. Ed.Engl. *58*, 2278–2283.

21. Volonakis, G., Filip, M.R., Haghighirad, A.A., Sakai, N., Wenger, B., Snaith, H.J., and Giustino, F. (2016). Lead-free halide double perovskites via heterovalent substitution of noble metals. J. Phys. Chem. Lett. *7*, 1254–1259.

22. Dahl, J.C., Osowiecki, W.T., Cai, Y., Swabeck, J.K., Bekenstein, Y., Asta, M., Chan, E.M., and Alivisatos, A.P. (2019). Probing the stability and band gaps of $Cs_2AgInCl_6$ and $Cs_2AgSbCl_6$ lead-free double perovskite nanocrystals. Chem. Mater. *31*, 3134–3143.

23. Zhao, X.G., Yang, D., Sun, Y., Li, T., Zhang, L., Yu, L., and Zunger, A. (2017). Cu-in halide perovskite solar absorbers. J. Am. Chem. Soc. *139*, 6718–6725.

24. Zhou, J., Rong, X., Molokeev, M.S., Zhang, X., and Xia, Z. (2018). Exploring the transposition effects on the electronic and optical properties of $Cs_2AgSbCl_6$ via a combined computational-experimental approach. J. Mater. Chem. *6*, 2346–2352.

25. Deng, W., Deng, Z.Y., He, J., Wang, M., Chen, Z.X., Wei, S.H., and Feng, H.J. (2017). Synthesis of $Cs_2AgSbCl_6$ and improved optoelectronic properties of $Cs_2AgSbCl_6$/TiO_2 heterostructure driven by the interface effect for lead-free double perovskites solar cells. Appl. Phys. Lett. *111*, 151602.

26. Guo, Y., Lou, Y., Chen, J., and Zhao, Y. (2022). Lead-free $Cs_2AgSbCl_6$ double perovskite nanocrystals for effective visible-light photocatalytic C-C coupling reactions. ChemSusChem *15*, e202102334.

27. Luo, J., Wang, X., Li, S., Liu, J., Guo, Y., Niu, G., Yao, L., Fu, Y., Gao, L., Dong, Q.S., et al. (2018). Efficient and stable emission of warm-white light from lead-free halide double perovskites. Nature *563*, 541–545.

28. Zhou, Y., Chen, J., Bakr, O.M., and Sun, H.T. (2018). Metal-doped lead halide perovskites: synthesis, properties, and optoelectronic applications. Chem. Mater. *30*, 6589–6613.

29. Akkerman, Q.A., Meggiolaro, D., Dang, Z., De Angelis, F., and Manna, L. (2017). Fluorescent alloy $CsPb_xMn_{1-x}I_3$ perovskite nanocrystals with high structural and optica stability. ACS Energy Lett. *2*, 2183–2186.

30. Locardi, F., Cirignano, M., Baranov, D., Dang, Z., Prato, M., Drago, F., Ferretti, M., Pinchetti, V., Fanciulli, M., Brovelli, S., et al. (2018). Colloidal synthesis of double perovskite $Cs_2AgInCl_6$ and Mn-doped $Cs_2AgInCl_6$ nanocrystals. J. Am. Chem. Soc. *140*, 12989–12995.

31. Vargas, B., Ramos, E., Pérez-Gutiérrez, E., Alonso, J.C., and Solis-Ibarra, D. (2017). A direct bandgap copper-antimony halide perovskite. J. Am. Chem. Soc. *139*, 9116–9119.

32. Bi, C., Wang, S., Li, Q., Kershaw, S.V., Tian, J., and Rogach, A.L. (2019). Thermally stable copper(II)-doped cesium lead halide perovskite quantum dots with strong blue emission. J. Phys. Chem. Lett. *10*, 943–952.

33. Karmakar, A., Dodd, M.S., Agnihotri, S., Ravera, E., and Michaelis, V.K. (2018). Cu(II)-doped $Cs_2SbAgCl_6$ double perovskite: a lead-free, low-bandgap material. Chem. Mater. *30*, 8280–8290.

34. Lei, F., Zhang, L., Sun, Y., Liang, L., Liu, K., Xu, J., Zhang, Q., Pan, B., Luo, Y., and Xie, Y. (2015). Atomic-layer-confined doping for atomic-level insights into visible-light water splitting. Angew. Chem. Int. Ed. Engl. *54*, 9266–9270.

35. Xu, H.Q., Hu, J., Wang, D., Li, Z., Zhang, Q., Luo, Y., Yu, S.H., and Jiang, H.L. (2015). Visible-light photoreduction of CO_2 in a metal-organic framework: boosting electron-hole separation via electron trap states. J. Am. Chem. Soc. *137*, 13440–13443.

36. Wang, M., Shen, M., Jin, X., Tian, J., Li, M., Zhou, Y., Zhang, L., Li, Y., and Shi, J. (2019). Oxygen vacancy generation and stabilization in CeO_{2-x} by Cu introduction with improved CO_2 photocatalytic reduction activity. ACS Catal. *9*, 4573–4581.

37. Wu, J., Li, X., Shi, W., Ling, P., Sun, Y., Jiao, X., Gao, S., Liang, L., Xu, J., Yan, W., et al. (2018). Efficient visible-light-driven CO_2 reduction mediated by defect-engineered BiOBr atomic layers. Angew. Chem. Int. Ed. Engl. *57*, 8719–8723.

38. Zhang, H.-X., Hong, Q.-L., Li, J., Wang, F., Huang, X., Chen, S., Tu, W., Yu, D., Xu, R., Zhou, T., and Zhang, J. (2019). Isolated square-planar copper center in boron imidazolate nanocages for photocatalytic reduction of CO_2 to CO. Angew. Chem. Int. Ed. Engl. *58*, 11752–11756.

39. Sheng, J., He, Y., Li, J., Yuan, C., Huang, H., Wang, S., Sun, Y., Wang, Z., and Dong, F. (2020). Identification of halogen-associated active sites on bismuth-based perovskite quantum dots for efficient and selective CO_2-to-CO photoreduction. ACS Nano *14*, 13103–13114.

40. Liu, L., and Li, Y. (2014). Understanding the reaction mechanism of photocatalytic reduction of CO_2 with H_2O on TiO_2-based photocatalysts: a review. Aerosol Air Qual. Res. *14*, 453–469.

41. Li, N., Wang, B., Si, Y., Xue, F., Zhou, J., Lu, Y., and Liu, M. (2019). Toward high-value hydrocarbon generation by photocatalytic reduction of CO_2 in water vapor. ACS Catal. *9*, 5590–5602.

42. Rodrigues, J.E.F.S., Escanhoela, C.A., Jr., Fragoso, B., Sombrio, G., Ferrer, M.M., Álvarez-Galván, C., Fernández-Díaz, M.T., Souza, J.A., Ferreira, F.F., Pecharromán, C., and Alonso, J.A. (2021). Experimental and theoretical investigations on the structural, electronic, and vibrational properties of $Cs_2AgSbCl_6$ double perovskite. Ind. Eng. Chem. Res. *60*, 18918–18928.

43. Henkelman, G., Arnaldsson, A., and Jónsson, H. (2006). A fast and robust algorithm for Bader decomposition of charge density. Comput. Mater. Sci. *36*, 354–360.

44. Sanville, E., Kenny, S.D., Smith, R., and Henkelman, G. (2007). Improved grid-based algorithm for Bader charge allocation. J. Comput. Chem. *28*, 899–908.

45. Chernyshova, I.V., Ponnurangam, S., and Somasundaran, P. (2013). Linking interfacial chemistry of CO_2 to surface structures of hydrated metal oxide nanoparticles: hematite. Phys. Chem. Chem. Phys. *15*, 6953–6964.

46. Corson, E.R., Kas, R., Kostecki, R., Urban, J.J., Smith, W.A., McCloskey, B.D., and Kortlever, R. (2020). In situ ATR-SEIRAS of carbon dioxide reduction at a plasmonic silver cathode. J. Am. Chem. Soc. *142*, 11750–11762.

47. Zhang, R., Wang, H., Tang, S., Liu, C., Dong, F., Yue, H., and Liang, B. (2018). Photocatalytic oxidative dehydrogenation of ethane using CO_2 as a soft oxidant over Pd/TiO_2 catalysts to C_2H_4 and Syngas. ACS Catal. *8*, 9280–9286.

48. Yu, X., Yang, Z., Qiu, B., Guo, S., Yang, P., Yu, B., Zhang, H., Zhao, Y., Yang, X., Han, B., and Liu, Z. (2019). Eosin Y-functionalized conjugated organic polymers for visible-light-driven CO_2 reduction with H_2O to CO with high efficiency. Angew. Chem. Int. Ed. Engl. *58*, 632–636.

49. Fisher, I.A., and Bell, A.T. (1998). In situ infrared study of methanol synthesis from H_2/CO over Cu/SiO_2 and Cu/ZrO_2/SiO_2. J. Catal. *178*, 153–173.

50. Fujita, S.i., Nakamura, M., Doi, T., and Takezawa, N. (1993). Mechanisms of methanation of carbon-dioxide and carbon-monoxide over nickel alumina catalysts. Appl. Catal. A *104*, 87–100.

51. Sheng, P.Y., Yee, A., Bowmaker, G.A., and Idriss, H. (2002). H_2 production from ethanol over Rh-Pt/CeO_2 catalysts: the role of Rh for the efficient dissociation of the carbon-carbon bond. J. Catal. *208*, 393–403.

52. Cui, S., Cheng, W., Shen, X., Fan, M., Russell, A.T., Wu, Z., and Yi, X. (2011). Mesoporous amine-modified SiO_2 aerogel: a potential CO_2 sorbent. Energy Environ. Sci. *4*, 2070–2074.

53. Sheng, J., He, Y., Huang, M., Yuan, C., Wang, S., and Dong, F. (2022). Frustrated lewis pair sites boosting CO_2 photoreduction on Cs_2CuBr_4 perovskite quantum dots. ACS Catal. *12*, 2915–2926.

54. Nørskov, J.K., Rossmeisl, J., Logadottir, A., Lindqvist, L., Kitchin, J.R., Bligaard, T., and Jónsson, H. (2004). Origin of the overpotential for oxygen reduction at a fuel-cell cathode. J. Phys. Chem. B *108*, 17886–17892.

STAR★METHODS

KEY RESOURCES TABLE

REAGENT or RESOURCE	SOURCE	IDENTIFIER
Chemicals, peptides, and recombinant proteins		
CsCl	Aladdin	7647-17-8
AgCl	Sigma Aldrich	7783-90-6
$CuCl_2 \cdot 2H_2O$	Aladdin	10125-13-0
$SbCl_3$	Aladdin	10025-91-9
HCl	Aladdin	7647-01-0
C_2H_5OH	Aladdin	64-17-5

RESOURCE AVAILABILITY

Lead contact

Further information and requests for resources and materials should be directed to and will be fulfilled by the lead contact, Prof. Xiaosheng Tang (xstang@cqu.edu.cn).

Materials availability

This study did not generate new unique reagents.

Data and code availability

- Data reported in this paper will be shared by the lead contact upon request.
- This paper does not report original code.
- Any additional information required to reanalyze the data reported in this paper is available from the lead contact upon request.

METHOD DETAILS

Synthesis of the $Cs_2AgSbCl_6$ microcrystals

$Cs_2AgSbCl_6$ microcrystals are synthesized via solution-state reaction. Starting materials 1 mmol of $SbCl_3$ and an equal amount of AgCl are dissolved in the 12ml HCl and heated to 80 °C under the continuous stirring. Then, 2 mmol of CsCl is added in the hot solution. Soon after, the yellow precipitate is formed in the bottom of the flask. The precipitate is collected and washed with ethanol three times, then dried at 150 °C in the air for 7 h. After cooling to room temperature, the yellow powder is obtained.

Synthesis of the Cu doped $Cs_2AgSbCl_6$ microcrystals

0.034 g of $CuCl_2 \cdot 2H_2O$ (0.20 mmol) was dissolved in 5 mL of 10 M HCl and a homogeneous solution was obtained. In a separate reaction, 1 mmol of SbCl3 and an equal amount of AgCl are dissolved in the 12ml HCl and heated to 80°C under the continuous stirring. Following dissolution, 2 mmol of CsCl and x mL of $CuCl_2 \cdot 2H_2O$, prepared as described above, were added to the solution. The polycrystalline solid was washed with ethanol, and then dried at 150°C in the air for 7 h.

Characterization

X-ray diffraction (XRD) spectra of the samples was decided by powder X-ray diffraction (XRD) with Cu Kα (0.154178 nm) radiation (MADZU, Japan). The scanning electronic microscopy (SEM) were examined on Quattro S with high resolution Schottky field emission electron gun (Thermo Fisher Scientific). The transmission electron microscopy (TEM) and high-resolution transmission electron microscopy (HRTEM) were examined on ZEISS LIBRA 200FE. The inductively coupled plasma optical emission spectrometer (ICP-OES) iCAP 6300 Duo was used to analysis the content of elements in double perovskites. The UV-visible absorption spectrum was determined by the scan UV-VIS-NIR spectrophotometer (UV-2100) (Japan)

from 300 to 1100 nm. X-ray photoelectron spectroscopy (XPS) determined the chemical states of samples on ESRCALAB250Xi, Thermo Fisher Scientific. The binding energies were referenced to the C 1s peak at a binding energy of 284.8 eV. CO_2 adsorption isotherms measurements were carried out by using an automatic microporous physical and chemical gas adsorption analyzer (ASAP 2020 V3.04 H). The perovskites thin film is fabricated by spin-coating process. The ITO substrates (1.5 * 1.5 cm) were cleaned by sonicating sequentially in deionized water, alcohol and acetone, each for 10 min. The washed perovskites toluene suspension was then spin-coated on the ITO substrates at 2000 rpm for 30 s. The as-prepared thin films were subsequently dried at 60°C on a hotplate to completely evaporate any residual supernatant. The photoelectrochemical experiments were performed on the CHI760e in a 3-electrode configuration with the assembled photoelectrodes (perovskite on ITO glass) as the working electrode, the Pt mesh as the counter electrode and the Ag/AgCl electrode as the reference electrode. Filling the ethyl acetate with 0.1 M tetrabutylammonium hexafluorophosphate ($TBAPF_6$) in the cell can be taken as electrolyte. In an isotope labelling experiment, the CO products were detected by differentially pumped quadrupole mass spectrometer (QMS, Hiden HPR20).

Photocatalytic CO_2 reduction

Photocatalytic CO_2 decrease was carried out at the Labsolar-6A system (Perfect Light Co., China). Meanwhile, the system is made up of a fully-enclosed quartzose reactor, a 300 W Xe lamp, and gas chromatography (GC). Before carrying out catalysis, the Xe lamp was configured for the simulation of the illumination of the solar light. The measurements were carried out within a 40 mL sealed Pyrex bottle filled with CO_2 and H_2O vapor. During the representative progress, the ultrasonic dispersion of 2 mg photocatalyst was made in 1.0 mL toluene. Then, the mixture solution was applied onto a glass (2.0 * 2.0 cm) and heated to 100°C in ambient atmosphere for 0.5 hours to remove the extraneous toluene. The treated clean sample films and 100 μL water were put into the bottle which was degassed repeatedly to remove air and then filled with CO_2. In the reaction, the analysis of gaseous products collected was made per hour by a gas chromatography. The CO_2 gas had the purity of 99.999% and reaction pressure of 85∼90 kPa.

Ultrafast transient absorption

TA experiments were carried out using a home-made femtosecond pump-probe setup. The pump light is generated by injecting the femtosecond laser from the Ti: sapphire amplifier to the optical parametric amplifier, using the signal pulse and the double frequency of the 780 nm light, then half chopped to 500 Hz. The probe light is generated by injecting the 800 nm pulses (1 kHz) into Sapphire crystals, thus generating smooth super continuum. Diameter of the pump light on the sample is 340 μm, and 120 μm for the probe light. The TA signal is obtained by calculating the absorption difference of the sample on the probe light with and without pump light, namely, ΔA = A01− A00, where A01 absorptance with the pump, and A00 is the delay time related is the absorptance without the pump.

In-situ FT-IR investigation on photocatalytic CO_2 reduction

In-situ FT-IR measurements were carried out at a BRUKER TENSOR 27 Fourier transform infrared spectrometer instrument equipped with a tailor-made reactor and liquid nitrogen cooled HgCdTe (MCT) detector. Before the adsorption/desorption process, the loaded samples were purged with Ar (50 mL min^{-1}) for 1 h at 120°C to sweep all the impurities. Then, the background spectrum was collected after the chamber temperature was lowered to room temperature. Next, the mixed reaction gas flow (25 ml min^{-1} of Ar and 5 ml min^{-1} of CO_2 with a trace of H_2O vapor) was introduced into the reactor, and the variation of FT-IR spectra was recorded to monitor the dynamic adsorption process. After reaching the sorption equilibrium (∼30 min), the background spectrum was collected again. Afterward, turn on the light irradiation (300 W Xe lamp), and the FT-IR spectra were recorded as a function of time to investigate the dynamics of the conversion of the reactants under irradiation.

Computational details

First-principles computations were accomplished with the projector augmented wave (PAW) formalism as performed using the Vienna ab initio simulation package (VASP). The Perdew-Burke-Ernzerhof (PBE) generalized gradient approximation (GGA) functional was employed to model the exchange-correlation interactions, including vdW correction with the DFT-D3 method. Plane-wave cutoff of 500 was set for

all the computations in this study and spin-polarization was included. We built a 1×1×1 supercell of the flat surface $Cs_2AgSbCl_6$ slab with a vacuum of 20 Å. The top three layers of the slab surfaces including adsorbates were relaxed in the calculations, while the bottom two layers were fixed. The k-point sampling in the Brillouin zone was implemented using the Monkhorst-Pack scheme with grids 3×3×1 and 5×5×1 for the geometric optimization and energy calculation, respectively. The convergence criteria of energy and forces acting on each atom were 10^{-5} eV and 0.02 eV $Å^{-1}$, respectively, in the geometry optimization.

In order to build the Gibbs free energy diagram, the computational hydrogen electrode (CHE) model was used where each electrochemical reaction step is treated as a simultaneous transfer of the proton-electron pair as a function of the applied potential. The proposed reaction paths during the CO_2 photoreduction on the surface are shown below:

$$CO_2(g) + * + H^+(aq) + e^- \leftrightarrow *COOH$$

$$*COOH + H^+(aq) + e^- \leftrightarrow *CO + H_2O(l)$$

$$*CO + e^- + H^+ \rightarrow *HCO(g) \text{ or } *CO \rightarrow CO\uparrow + *$$

$$*HCO + e^- + H^+ \rightarrow *HCHO$$

$$*HCHO + e^- + H^+ \rightarrow *CH_2OH \text{ or } *HCHO \rightarrow HCHO\uparrow + *$$

$$*CH_2OH + e^- + H^+ \rightarrow *CH_3OH$$

$$*CH_3OH + e^- + H^+ \rightarrow *CH_3 + H_2O \text{ or } *CH_3OH \rightarrow CH_3OH\uparrow + *$$

$$*CH_3 + e^- + H^+ \rightarrow *CH_4$$

$$*CH_4 \rightarrow CH_4\uparrow + *$$

where "*" is the active site. Using the initial state where gaseous CO_2 molecules are freely above an empty surface as the reference, the Gibbs free energy changes of interest can finally be represented as,

$$\Delta G[*COOH] = G[*COOH] - (G[*] + G[CO_2] + 1/2G[H_2])$$

$$\Delta G[*CO] = G[*CO] + G[H_2O] - (G[*COOH] + 1/2G[H_2])$$

$$\Delta G[CO] = G[CO] - G[*CO]$$

$$\Delta G[*HCO] = G[*HCO] - (G[*CO] + 1/2G[H_2])$$

$$\Delta G[*HCHO] = G[*HCHO] - (G[*HCO] + 1/2G[H_2])$$

$$\Delta G[HCHO] = G[HCHO] - G[*HCHO]$$

$$\Delta G[*CH_2OH] = G[*CH_2OH] - (G[*HCHO] + 1/2G[H_2])$$

$$\Delta G[*CH_3OH] = G[*CH_3OH] - (G[*HCH_2O] + 1/2G[H_2])$$

$$\Delta G[CH_3OH] = G[CH_3OH] - G[*HCH_3O]$$

$$\Delta G[*CH_3] = G[*CH_3] + G[H_2O] - (G[*HCH_3O] + 1/2G[H_2])$$

$$\Delta G[CH_4] = G[CH_4] - (G[*CH_3] + 1/2G[H_2])$$

To build the Gibbs free energy diagram with the computational hydrogen electrode model, Gibbs free energies for relevant species were calculated with the expression:

$$G = E_{DFT} + E_{ZPE} - TS$$

where E_{DFT} is the calculated DFT electronic energy, E_{ZPE} is the zero-point vibrational energy. TS is the entropy contribution. All the calculated thermodynamic parameters used to build Gibbs free energy diagrams are listed in Table S4.